



N₂O decomposition over ceria-promoted Ir/Al₂O₃ catalysts: The role of ceria



E. Pachatouridou^{a,b}, E. Papista^c, A. Delimitis^b, M.A. Vasiliades^d, A.M. Efstathiou^{d,*},
M.D. Amiridis^e, O.S. Alexeev^f, D. Bloom^g, G.E. Marnellos^{b,c}, M. Konsolakis^{a,*},
E. Iliopoulou^{b,*}

^a School of Production Engineering and Management, Technical University of Crete, GR-73100 Chania, Crete, Greece

^b Chemical Process & Energy Resources Institute (CPERI), Centre for Research & Technology Hellas (CERTH), 6th km. Charilaou–Thermi Rd., P.O. Box 60361, GR-57001, Thermi, Thessaloniki, Greece

^c Department of Mechanical Engineering, University of Western Macedonia, Bakola & Sialvera, GR-50100, Kozani, Greece

^d Heterogeneous Catalysis Laboratory, Department of Chemistry, University of Cyprus, P.O. Box 20537, 1678 Nicosia, Cyprus

^e University of Illinois at Chicago, IL, 60607 Chicago, USA

^f Department of Chemical Engineering, University of South Carolina, SC, 29208 Columbia, USA

^g Electron Microscopy Center, University of South Carolina, SC, 29208 Columbia, USA

ARTICLE INFO

Article history:

Received 13 October 2015

Received in revised form 14 January 2016

Accepted 20 January 2016

Available online 22 January 2016

Keywords:

N₂O decomposition

Ir/Al₂O₃ catalysts

Ceria promotion

HAADF-STEM/EELS

CO-DRIFTS

ABSTRACT

The impact of CeO₂ in the Al₂O₃–20 wt% CeO₂ support prepared by the co-precipitation method on the Ir particle size, morphology and oxidation state, and in turn on the deN₂O catalytic activity (1000 ppm N₂O) of supported Ir catalysts were investigated in the absence and presence of excess O₂ (2 vol%) conditions. It was demonstrated that the deN₂O activity of Ir/Al₂O₃ is notably suppressed by the presence of oxygen in the feed stream, namely, the N₂O conversion at 600 °C is declined to 65% in the presence of oxygen as compared to 100% in the absence of oxygen. A similar detrimental catalytic effect was also observed for the Ir/CeO₂ solid. On the contrary, the deN₂O performance of CeO₂-modified Ir/Al₂O₃ catalyst is only slightly affected by the presence of oxygen. An extensive characterization study involving surface texture analysis (N₂ adsorption-desorption at –196 °C), temperature-programmed reduction in H₂ (H₂-TPR), X-ray diffraction (XRD), high resolution transmission electron microscopy (HRTEM), scanning transmission electron microscopy (STEM), electron energy loss spectroscopy (EELS) and diffuse reflectance infrared Fourier transform spectroscopy of CO adsorption and desorption (CO-DRIFTS) was carried out to gain insight into the origin of the CeO₂-induced promotional effect. The characterization results revealed the existence of IrO₂ phase (H₂-TPR, XRD, HRTEM, EELS and CO-DRIFTS) as well as of very small isolated particles of Ir on the Al₂O₃, CeO₂ and CeO₂–Al₂O₃ supports (STEM) but to a notably different extent. The coexistence of large IrO₂ particles of perfect crystallite structure and very small Ir particles located at the Ir-ceria interface was revealed only in Ir/AlCe. The establishment of a certain Ir^{δ+}/Ir⁰ ratio and oxygen vacant sites (V_O) concentration in ceria around very small Ir particles under oxidative reaction conditions seem to largely promote N₂O adsorption and subsequent decomposition into N₂ and O₂ over the CeO₂-promoted Ir/Al catalyst. In the case of Ir/Al, a different deN₂O decomposition mechanism occurs, where the site reactivity of Ir^{δ+}/Ir⁰ established under oxidizing conditions is reduced significantly.

© 2016 Elsevier B.V. All rights reserved.

1. Introduction

Nitrous oxide (N₂O) has long been considered as a relatively harmless substance. However, during the last years a growing con-

cern has been developed focusing on its abatement, since N₂O has been recognized as a powerful greenhouse gas with a long lifetime (~150 years in the atmosphere) and a Global Warming Potential (GWP) of ~300 times higher than that of CO₂ [1,2]. Furthermore, it has been well established that nitrous oxide participates in the chemical cycle leading to the destruction of ozone layer [1–4].

Due to the negative effects of N₂O on the global environment, its emissions control from anthropogenic sources, such as the combustion of fossil fuels and biomass in stationary and transport applications, and the nitric and adipic acid chemical production,

* Corresponding authors.

E-mail addresses: efstath@ucy.ac.cy (A.M. Efstathiou), mkonsol@science.tuc.gr (M. Konsolakis), eh@certh.gr (E. Iliopoulou).

URL: <http://www.tuc.gr/konsolakis.html> (M. Konsolakis).

where flue gas treatment is feasible, should be put forward [5,6]. N₂O abatement can be achieved either by preventing its formation or by applying end-of-pipe technologies, such as thermal decomposition, plasma technology, selective adsorption and catalytic decomposition [7–10]. The catalytic decomposition of N₂O into nitrogen and oxygen consists one of the most efficient methods for N₂O abatement due to the lower energy requirements and consequently lower associated cost compared to thermal and plasma technologies [5,11–13].

Various types of catalysts were found capable to decompose N₂O, including supported noble metals (NMs) [13,14], metal oxides [15,16] and zeolites [17]. Among these groups of catalysts, NMs supported catalysts exhibit satisfactory activity even at low temperatures. Especially, Rh-based catalysts were reported to catalyze N₂O decomposition at temperatures typically lower than 400 °C [18,19]. Interestingly, Rh₂O₃ has been recently identified as a highly active phase for N₂O decomposition by experimental [19] and theoretical studies [20]. On the contrary, in the case of Pt-based catalysts, the N₂O decomposition is drastically hindered by the adsorbed oxygen (N₂O/O₂/He feed gas mixture) leading to complete deactivation over fully oxidized Pt surface [21,22].

Recently, great attention has been devoted on the deNO_x activity of Ir-based catalysts, because of their lower cost and peculiar physicochemical properties as compared to conventional Pt-, Pd- and Rh-based catalysts [23–40]. For example, Wang et al. [27,29] showed that Ir/ZSM-5 catalysts exhibit better performance as compared to Pt, Pd and Rh catalysts for the NO reduction by CO under O₂ excess conditions. In a similar manner, the enhanced catalytic activity of Ir/SiO₂ catalysts for the NO selective catalytic reduction with CO in the presence of O₂, H₂O and SO₂ was also reported [30,32,36]. Fujitani et al. [38] reported on the high NO dissociation activity of Ir (1 1 1) surface, which is retained even under high oxygen surface coverages [39,40].

The high cost of NMs presents an important obstacle toward the development of deN₂O catalytic technologies. In this regard, several strategies have been focused to enhance the intrinsic reactivity of noble metal-based catalysts via the use of structural and/or surface modifiers [41–47]. To this end, it has been recently shown that the deN₂O efficiency of Pt/Al₂O₃ catalysts can be greatly enhanced by the incorporation of CeO₂-La₂O₃ mixed oxides onto the Al₂O₃ support. In particular, complete conversion of N₂O was attained over Pt/Al₂O₃-(CeO₂-La₂O₃) catalysts at 500 °C, in contrast to the unmodified Pt/Al₂O₃ catalyst, which exhibited N₂O conversion values less than 20% at 600 °C [42]. Besides structural modifiers, electropositive promoters, such as alkali or alkaline earths, have been also reported to play a key role on the deN₂O process over several catalytic systems [41,44,45].

Very recently, the deN₂O performance of Pt-, Pd- and Ir-Al₂O₃ catalysts was investigated with particular emphasis on the impact of metal loading and reaction conditions [48]. The superiority of Al₂O₃-supported Ir catalysts was clearly revealed, where complete conversion of N₂O was achieved at about 600 °C in the absence of oxygen. On the contrary, Pt/Al₂O₃ catalysts were almost inactive below 600 °C irrespectively of the reaction conditions employed, whereas an intermediate performance was obtained for Pd/Al₂O₃ catalysts [48].

In the light of the above considerations, the present work aims at exploring the impact of ceria promotion on the deN₂O performance of 0.5 wt% Ir/CeO₂-Al₂O₃ catalysts. The effect of temperature and oxygen presence in the feed stream (N₂O/He vs. N₂O/O₂/He) on catalyst activity was examined. Several complementary characterization techniques, namely: BET, XRD, H₂-TPR, HRTEM, HAADF-STEM, EELS and CO-DRIFTS were employed in an effort to gain insight into possible structure-activity relationships.

2. Experimental

2.1. Materials synthesis

All support materials of Ir phase, namely: γ -Al₂O₃, CeO₂ and CeO₂-modified γ -Al₂O₃ (20 wt% CeO₂) were prepared by the co-precipitation method. A precipitating agent (25 vol% NH₃ solution) was added at room temperature to a continuously stirred solution containing the desirable amounts of Al(NO₃)₃·9H₂O (98.5% purity, supplied by Chem-Lab) and/or Ce(NO₃)₃·6H₂O (99% purity, supplied by Fluka), until the pH of the solution reached the value of ~10. The pH remained then stable at this value for additional 3 h. Following co-precipitation, the resulting precipitate was filtered, dried overnight at 110 °C and then calcined at 600 °C for 2 h in air flow.

The incorporation of the active metal phase on the Al₂O₃, CeO₂ or CeO₂-modified Al₂O₃ support was conducted by the incipient wetness impregnation method, using an aqueous solution of IrCl₃·H₂O (98% purity, supplied by Merck) so as to yield a nominal 0.5 wt% Ir loading. The impregnation step was followed by drying (100 °C, 12 h) and calcination (600 °C, 3 h) step in air flow. At 600 °C, no iridium loss is expected due to the extremely low volatility of IrO_x species [49]. Three samples were obtained from this procedure: the non-promoted 0.5 wt% Ir/Al₂O₃, ceria-promoted 0.5 wt% Ir/80 wt% Al₂O₃-20 wt% CeO₂ and 0.5 wt% Ir/CeO₂, which will be denoted hereinafter as Ir/Al, Ir/AlCe and Ir/Ce, respectively.

2.2. Characterization studies

The textural characteristics of the as prepared catalysts were determined by the N₂ adsorption-desorption isotherms at –196 °C (Nova 2200e Quantachrome flow apparatus). Specific surface areas (m² g^{–1}) were obtained according to the Brunauer-Emmett-Teller (BET) method at relative pressures in the 0.05–0.30 range. The specific pore volume (cm³ g^{–1}) was calculated based on the highest relative pressure, whereas the average pore size diameter (d_p , nm) was determined by the Barrett-Joyner-Halenda (BJH) method. Prior to measurements the samples were degassed at 350 °C for 5 h under vacuum.

The crystalline structure of the catalysts was determined by powder X-ray diffraction (XRD) on a Siemens D 500 diffractometer operated at 40 kV and 30 mA with Cu K α radiation (λ = 0.154 nm). Diffractograms were recorded in the 5–80° 2 θ range and at a scanning rate of 0.01° s^{–1}. The Scherrer equation was employed to determine the primary particle size of a given crystal phase based on the most intense diffraction peak.

Samples for electron microscopy (TEM, HRTEM, HAADF-STEM, EELS) characterization were prepared by gently grinding the catalyst powder in high-purity ethanol using an agate pestle and mortar. A drop of the solution was subsequently deposited onto a lacey carbon film supported on a Cu grid and allowed to evaporate under ambient conditions. Electron microscopy experiments were carried out in a JEOL 2011 high resolution transmission electron microscope (HRTEM), operating at 200 kV, with a point resolution of 0.23 nm. Elemental analysis was performed by means of energy-dispersive X-ray spectroscopy (EDS) using an Oxford Instruments spectrometer (INCAx-sight liquid nitrogen cooled detector with an ultrathin window). High resolution transmission electron microscopy (HRTEM) was performed using a JEOL 2100F 200 kV FEG-STEM/TEM spectrometer equipped with a CEOS Cs corrector on the illumination system. The geometrical aberrations were measured and controlled to provide a less than $\pi/4$ phase shift of the incoming electron wave over the probe-defining aperture of 17.5 mrad. High angle annular dark-field (HAADF-STEM) images were acquired on a Fischione Model 3000 HAADF detector with a camera length such that the inner cut-off angle of the detec-

tor was 50 mrad. The scanning acquisition was synchronized to the 60 Hz AC electrical power to minimize 60 Hz noise in the images and using a pixel dwell time of 15.8 μ s. EELS spectra were acquired in a probe-corrected 300 kV FEI Titan 3 G2 60–300 microscope with an X-FEG Schottky field emission electron source, equipped with a Gatan GIF Quantum ERS spectrometer.

Hydrogen temperature-programmed reduction (H_2 -TPR) experiments were performed after loading 0.1 g of sample in a quartz fixed bed reactor coupled with mass spectrometer (MS). A flow (50 cm³/min) of 5 vol% H_2 /He gas mixture was used, while the temperature of the solid catalyst was increased to 700 °C at the rate of 5 °C/min. The effluent gas from the reactor was analyzed using the MS detector ($m/z = 2$ was used for H_2). The as prepared sample in calcined state was loaded to the reactor and pre-treated at 300 °C for 1 h under He flow (heating rate of 3 °C/min from 30 to 300 °C). The catalyst sample was then cooled in He gas flow to room temperature before recording the H_2 -TPR trace.

In situ diffuse reflectance infrared Fourier transform spectroscopy (DRIFTS) experiments were carried out in a Perkin-Elmer/Frontier FT-IR spectrometer equipped with an MCT detector and a high-temperature/high-pressure controllable DRIFTS cell (Harrick Scientific), loaded with ~ 100 mg of catalyst sample (fine powder). Before DRIFT spectra acquisition, the as synthesized sample was pre-treated according to the following gas sequence: (i) 20 vol% O_2 /Ar (30 cm³/min) at 600 °C for 1 h (oxidation step), (ii) decrease of temperature to 300 °C in Ar flow, (iii) H_2 (1 bar) at 300 °C for 1 h (reduction step), and (iv) Ar purge at 300 °C, 10 min. Background spectra were recorded under Ar flow at desired temperatures (needed for CO desorption studies). CO chemisorption took place at 30 °C for 30 min with 1 vol% CO/He (30 cm³/min) gas mixture, whereas desorption of CO was performed in Ar flow (30 cm³/min). DRIFT-CO spectra under the desorption step were recorded after 2 min the catalyst sample reached the selected desorption temperature.

2.3. Catalytic activity measurements

N_2O catalytic decomposition activity experiments were performed in a cylindrical quartz U-shape fixed-bed reactor (inner diameter of 8 mm). The reactor was loaded with 0.1 g of catalyst (less than 0.3 mm in size) diluted with 0.05 g of quartz. The total gas flow rate was 150 cm³ (STP)/min, corresponding to a Gas Hourly Space Velocity (GHSV) of ~ 40000 h⁻¹. The feed composition was 1000 ppm N_2O or 1000 ppm $N_2O + 2$ vol% O_2 , balanced with He. Before catalytic activity measurements, the fresh calcined sample (see Section 2.1) was pretreated in He flow (100 cm³/min) for 1 h at 600 °C before cooled in He flow to the lowest reaction temperature. The N_2O conversion was monitored in the 200–600 °C range (in an increasing solid catalyst temperature mode). The composition of the effluent gas from the reactor was analyzed using a gas chromatograph (Shimadzu 14B) equipped with a thermal conductivity detector (TCD) and a combination of Porapak QS and Molecular Sieve 5A columns.

3. Results

3.1. Characterization studies

3.1.1. Textural characterization

Table 1 provides the textural characteristics (BET surface area, specific pore volume and pore size) of the Ir/Al, Ir/Ce and Ir/AlCe solids. It is obvious that alumina-based samples (Ir/Al and Ir/AlCe) possess similar textural characteristics. However, ceria-modified Ir catalyst (Ir/AlCe) presents a five-fold larger mean particle size of IrO_2 , as verified by XRD and HRTEM analyses to be presented

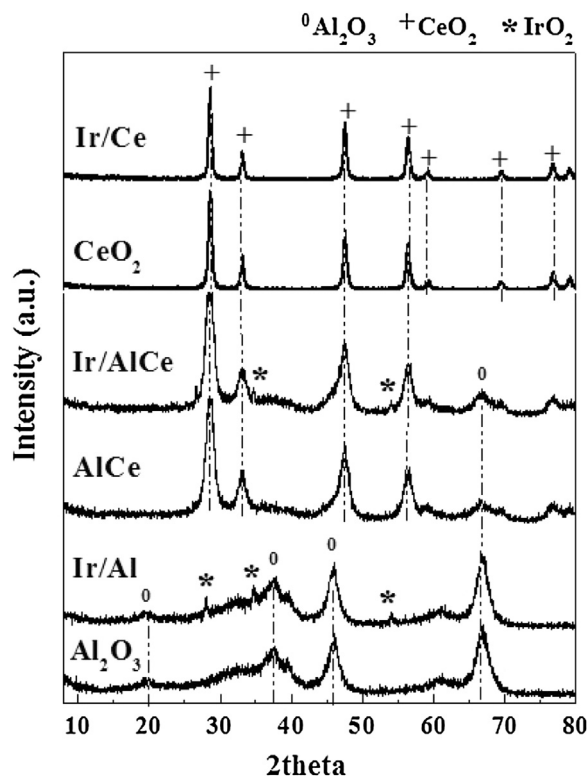


Fig. 1. Powder X-ray diffraction patterns of γ - Al_2O_3 , CeO_2 and Al_2O_3 -20 wt% CeO_2 (AlCe) bare supports and of the corresponding Ir supported metal catalysts.

next. This difference will be further discussed based on characterization and catalytic activity evaluation studies. On the other hand, ceria-based sample (Ir/Ce) presents the lowest BET area with a significantly lower pore volume as compared to the other two catalysts. Moreover, Ir/Al and Ir/Ce samples demonstrate a similar IrO_2 mean particle size according to HRTEM analyses (see Section 3.1.3).

3.1.2. Structural characterization (powder XRD)

Powder XRD patterns of iridium supported on γ - Al_2O_3 , CeO_2 and CeO_2 -modified γ - Al_2O_3 fresh calcined catalysts (see Section 2.1) are presented in Fig. 1. The presence of IrO_2 phase is confirmed by the XRD peaks appeared at 2θ : 28°, 34.7° (main peak) and 54° in the Ir/Al and Ir/AlCe samples [47]. In the case of CeO_2 -modified alumina catalyst, the IrO_2 peak at $2\theta = 28^\circ$ overlaps with the intense peak at $2\theta = 28.5^\circ$ of CeO_2 . The remaining diffraction peaks are characteristic of pure γ - Al_2O_3 (2θ : 37.7°, 46°, 67°) and CeO_2 (2θ : 33.3°, 47.5°, 56.4°, 76.5°) phases, as revealed by their corresponding XRD diffractograms [48,50].

The XRD pattern of Ir/Ce catalyst did not show diffraction peaks due to IrO_2 . Only the diffraction peaks of bare ceria with the fluorite structure were recorded. The absence of IrO_2 diffraction lines seems to be related with the large number density of small in size IrO_2 particles compared to that of large in size IrO_2 particles deposited on the surface of CeO_2 support, given also the low metal loading (0.5 wt% Ir) used, resulting, therefore, in very low-intensity diffraction peaks (Fig. 1). To this end, the broadening of diffraction peaks due to particle size effects also contributed to the absence of IrO_2 diffraction peaks. It is worth mentioning that the IrO_2 phase was clearly identified by powder XRD only in Ir/Al and Ir/AlCe samples, apparently due to the favourable distribution of IrO_2 particle size, as verified by HRTEM analysis (see Section 3.1.3). Measurements of the IrO_2 mean particle size (employing the Scherrer equation) resulted in 27 and 137 nm for the Ir/Al and Ir/AlCe catalysts, respectively, in

Table 1
Textural and redox (H_2 -TPR) characteristics of supported Ir catalysts.

Catalyst	S_{BET} (m ² /g)	Pore Volume (cm ³ /g)	Pore Size (nm)	Mean Ir particle size (nm)		T_{max} (°C) ^a	H_2 consumption (μmol/g) ^b
				XRD	TEM		
Ir/Al	182	0.32	6.9	27	31	223	19.6
Ir/Ce	27	0.06	8.3	–	27	216	89.7
Ir/AlCe	170	0.26	6.2	137	155 ^c	222	25.5

^a Temperature at maximum reduction rate (H_2 -TPR).

^b H_2 consumption as determined by H_2 -TPR in the low-T range of 150–250 °C (1st reduction peak).

^c Significant number density of tiny Ir clusters was also observed on top of IrO₂ and AlCe surfaces (Section 3.1.3).

good agreement with the TEM particle size analyses performed (31 and 155 nm, respectively). Despite the fact that the Ir/Ce powder XRD pattern did not show clear diffraction lines due to IrO₂ (main peak at 34.7°), the existence of this phase was verified by HRTEM analysis. The mean particle size of IrO₂ was similar to that of Ir/Al catalyst (Table 1).

3.1.3. Morphological studies (HRTEM, STEM, EELS)

The morphology, crystalline structure and particle size distribution of Ir supported metal catalysts (fresh samples calcined at 600 °C, see Section 2.1) were evaluated by means of HRTEM and STEM studies. Typical images of the Ir/Al sample are depicted in Fig. 2a and b. The alumina support comprises of small primary crystallites with sizes up to 20 nm, and a moderate degree of crystallinity, as shown by the rings in the selected area diffraction (SAD) pattern (Fig. 2a, inset I). On top of γ -Al₂O₃, large IrO₂ particles are observed (black arrows, Fig. 2a) with sizes up to 70 nm and a typical rectangular shape. The IrO₂ crystalline structure of these particles was proved by the discrete spots shown in the SAD pattern (inset I), where the main reflections for the tetragonal IrO₂ structure are indexed. The IrO₂ phase was also confirmed by EELS measurements (Fig. 2c), where a typical spectrum in the low loss regime (0–100 eV) is presented. The experimental peaks assigned to IrO₂ are located at 20.5, 28, 53.5 and 67 eV. Comparison with the theoretical EELS spectrum of IrO₂, superimposed at the same image, shows good agreement between the experimental peaks and those labeled as B, C, D and E in the theoretical spectrum, which confirms the presence of IrO₂. Besides the large in size crystalline IrO₂ particles, IrO₂ also appears as dense aggregates of smaller crystallites (inset II, Fig. 2a) with up to 10 nm in size as proved by SAD experiments in such regions. Measurements of the particle sizes of the two discrete IrO₂ morphologies over TEM micrographs (bimodal particle size distribution) resulted in a mean Ir particle size of 31 nm (see Table 1), which is in good agreement with that estimated from the XRD analysis.

To further elucidate the morphology of Ir particles in the calcined 0.5 wt% Ir/Al sample, HAADF-STEM experiments were carried out. A typical image is presented in Fig. 2b. It is shown that part of the Ir phase is widely dispersed on the γ -Al₂O₃ support and appears either as isolated particles, or as tiny clusters of Ir (up to 1.5 nm in size). HAADF imaging experiments proved that both entities have pure metallic character, in contrast to distinct IrO₂ particles formed in other regions of the sample. This result is in good agreement with the H_2 -TPR studies, where multiple oxidation states of Ir were evidenced.

TEM imaging experiments coupled with EDS were also carried out on the calcined 0.5 wt% Ir/CeO₂ catalyst (not shown for brevity's sake). The results revealed a similar Ir particle morphology and distribution with the Ir/Al material. The Ir/Ce catalyst comprises of small-up to 15 nm-IrO₂ particles, densely aggregated on top of CeO₂, and larger (75–90 nm in size) IrO₂ particles. The latter, usually found isolated on CeO₂, are in somehow lower percentage in Ir/Ce compared with the Ir/Al solid.

Features of the morphology of the calcined 0.5 wt% Ir/AlCe solid are presented in Fig. 3. The TEM image (Fig. 3a) shows several IrO₂ large particles dispersed on the AlCe support. The latter comprises of single crystalline nanoparticles with sizes in the 3–9 nm range. On the other hand, the IrO₂ particles are significantly larger than those of support, having mean sizes of about 155 nm (larger sizes up to 500 nm were also observed). They are crystalline materials, as confirmed by the HRTEM image in Fig. 3a (inset), where the (1 1 0) crystal planes of IrO₂ are resolved with an average d spacing of 0.317 nm. The termination of lattice planes almost up to its free surface clearly denotes particle's perfect crystal structure. Segregation of smaller IrO₂ particles into dense aggregates has not been extensively observed in this sample; only very few cases were encountered with small IrO₂ nanoparticles densely aggregated on the AlCe support.

The existence of any possible additional Ir structural entities in the Ir/AlCe material has been evaluated by means of HAADF-STEM imaging (Fig. 3b). Besides IrO₂ large secondary particles as described above, very small isolated Ir particles are readily observed, which are widely dispersed all over the AlCe support's surface. Furthermore, these very small Ir particles do not show a tendency for cluster formation as in the Ir/Al sample, but they mainly appear as discrete entities, distributed either on top of the AlCe support or the large IrO₂ particles. It is important to mention here that the small Ir (metallic character) particles/clusters identified in Ir/Al and Ir/AlCe solids have persisted conversion into IrO₂ after calcination at 600 °C. The above described findings indicate that the surface characteristics of the co-precipitated CeO₂ and Al₂O₃ phases are responsible for the formation of both large IrO₂ crystallites and very small Ir particles on the surface of Ir/AlCe solid. Jóźwiak and Maniecki [51] have reported on the mechanism of IrCl₃·3H₂O thermal decomposition under oxidative conditions. The entire process can be divided into three not overlapped temperature regions [51]: dehydration (50–400 °C), dechlorination-reoxidation (650–750 °C) and dissociative deoxidation of IrO₂ above 900 °C. It is speculated that the temperature range of dechlorination-reoxidation could vary in the case of supported IrCl₃·3H₂O phase, as in the present work. Therefore, the presence of Ir⁰ phase may not be a surprise. The main morphological characteristics of the three solid catalysts are summarized in Table 2.

3.1.4. H_2 -TPR studies

H_2 -TPR profiles of supported Ir catalysts are presented in Fig. 4, whereas Table 1 reports the corresponding H_2 consumption (μmol H_2 g^{−1}) in the low-T range of 150–250 °C and the peak maximum temperature (T_{max}) of the main reduction peak. The non-promoted catalyst (Ir/Al) presents a well-defined reduction peak centred at ~223 °C. This peak is attributed to the reduction of IrO₂ phase [48,50,52–56]. Besides the reduction peak of iridium oxide, the H_2 -TPR profile of Ir/Al catalyst exhibits also a broad reduction peak (350–500 °C), which can be attributed to the reduction of smaller IrO₂ particles present on the alumina support, as revealed by TEM and HAADF-STEM analyses (Fig. 2a, inset II).

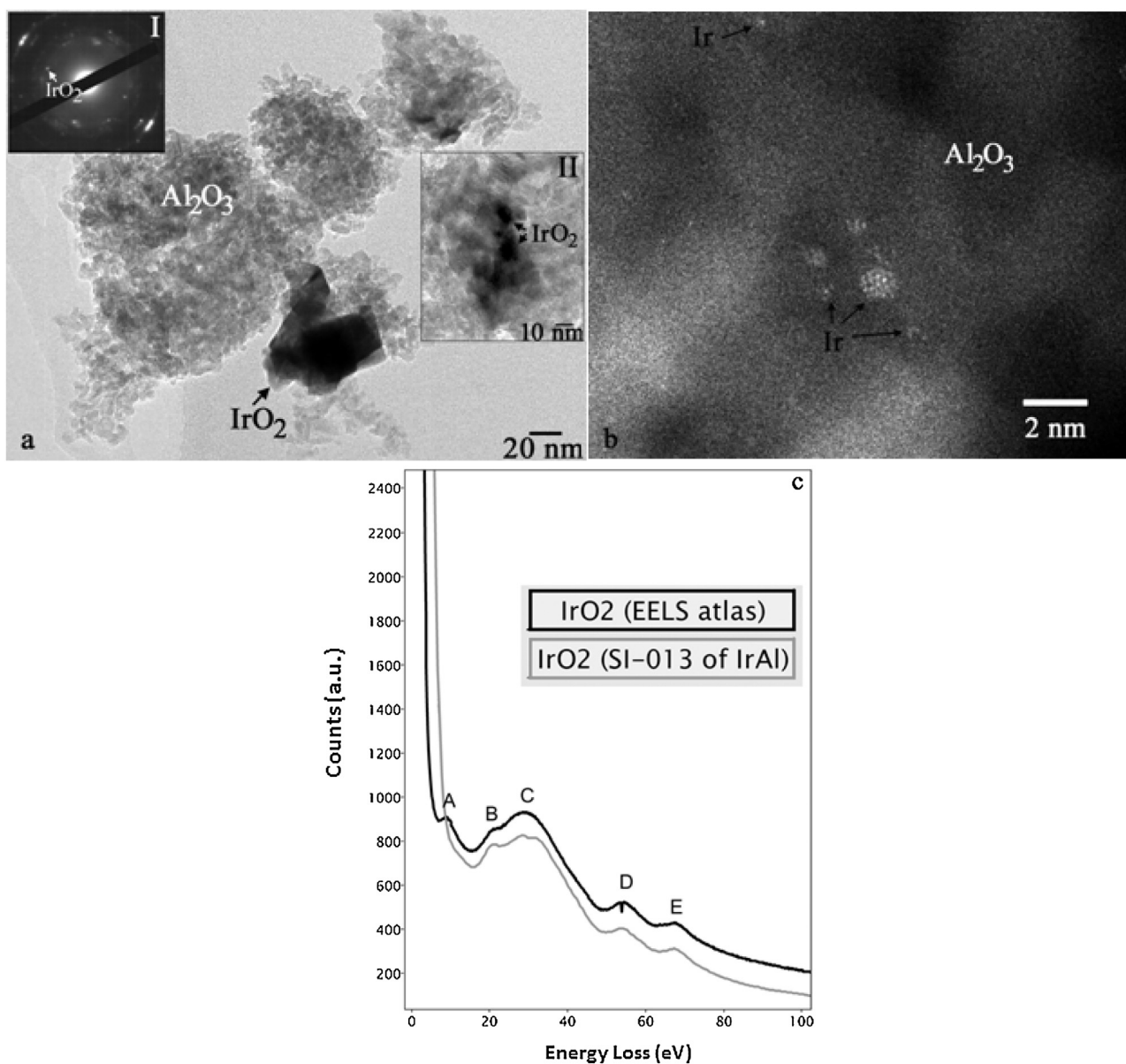


Fig. 2. (a) Electron microscopy images of Ir/Al catalyst, where a typical TEM BF image showing the IrO₂ discrete particles morphology is presented; (b) HAADF-STEM image, where isolated Ir metallic species are denoted with black arrows; (c) representative EELS spectrum of a large IrO₂ particle in the Ir/Al catalyst sample (grey line). The theoretical spectrum for IrO₂ [EELS Atlas by C.C. Ahn & O.L. Krivanek, Gatan (1983)] is also shown for comparison.

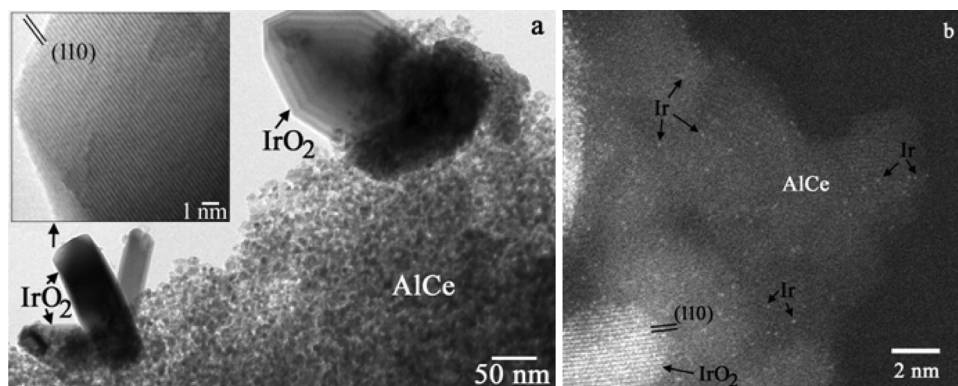


Fig. 3. Electron microscopy images of the Ir/AlCe catalyst: (a) TEM/HRTEM images revealing large IrO₂ particles, and (b) HAADF-STEM image revealing isolated very small Ir metallic particles (black arrowed), widely dispersed on top of the AlCe support and IrO₂ particles.

Table 2
Morphological characteristics of supported Ir catalysts.

Catalyst	Particles morphology			
	IrO ₂		Metallic Ir	
Ir/Al	Large crystallites (up to 70 nm)	Small crystallites (up to 10 nm) in dense aggregates	Isolated particles	Tiny clusters (up to 1.5 nm)
Ir/Ce	Large crystallites (up to 90 nm)	Small crystallites (up to 15 nm) in dense aggregates	–	–
Ir/AlCe	Large crystallites (up to 500 nm)	–	Isolated particles	–

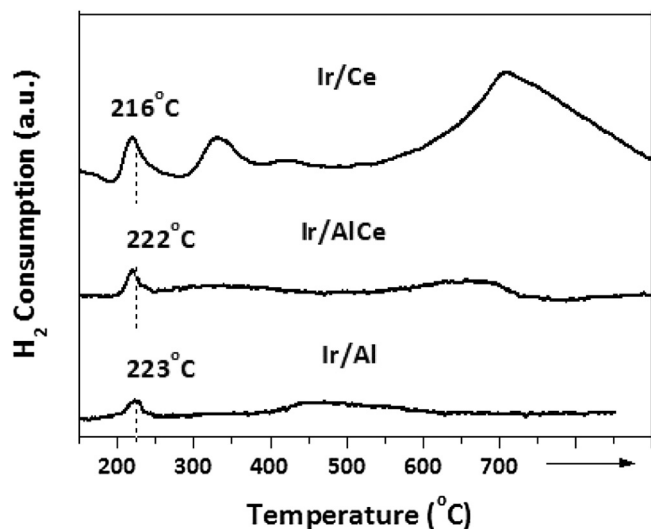


Fig. 4. H₂-TPR profiles of non-promoted (Ir/Al), CeO₂-promoted (Ir/AlCe) and Ir/CeO₂ (Ir/Ce) catalysts.

Modification of the Ir/Al with CeO₂ results in three reduction peaks: the first one is centered at 222 °C, and the two other broad peaks at 340 and 655 °C. The first low-T peak is largely related with the reduction of larger IrO₂ particles; reduction of surface Ce⁴⁺ → Ce³⁺ within few lattice constants around the Ir–CeO₂ interface cannot be excluded. The second broad peak at 340 °C can be assigned to further reduction of surface ceria facilitated by the presence of Ir. It has been reported [50] that incorporation of Ir metal on the CeO₂ support facilitates reduction of ceria surface due to metal-support interactions developed, resulting in H₂-TPR peaks at temperatures lower than 400 °C. Moreover, this peak could also be assigned to highly dispersed IrO₂ phase in close interaction with the support [57]. This finding is in line with the HAADF-STEM results (Fig. 3), which indicate the formation of very small Ir particles on the AlCe surface. The third broad reduction peak at high temperatures (ca. 655 °C) is related with the removal of bulk lattice oxygen from the CeO₂ matrix [57,58].

The Ir/CeO₂ catalyst (Ir/Ce) exhibits three reduction peaks (ca. 216, 330 and 707 °C). The first peak is attributed (see above) to the reduction of larger IrO₂ particles as in the case of the other two catalyst samples, but also to the ceria surface reduction around the IrO₂ particles. The second reduction peak is related with the reduction of small in size IrO₂ particles and ceria surface reduction, whereas the third high-T peak corresponds to the reduction of bulk ceria [57,58].

To gain further insight into the impact of CeO₂ on the redox properties of the catalysts, the H₂ consumption in the low-temperature range was estimated, where reduction of larger IrO₂ particles mainly occurs, and this is reported in Table 1. The non-promoted catalyst (Ir/Al) was found to consume 19.6 μmol H₂ g^{−1}, which corresponds to 37.7% reduction of the IrO₂ phase (0.5 wt% Ir). The corresponding percentage on Ir/AlCe is 49%. These results could imply either the promoting effect of CeO₂ towards the forma-

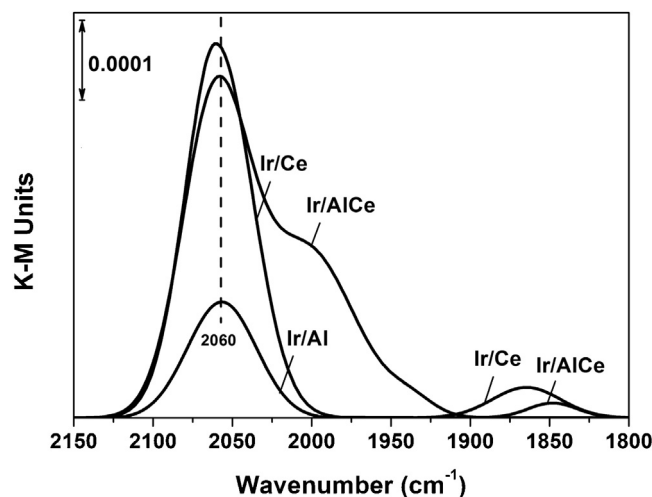


Fig. 5. *In situ* DRIFTS-CO spectra recorded on Ir/Al, Ir/Ce and Ir/AlCe catalysts following 30-min CO adsorption (1 vol% CO/He) at 30 °C and a 5-min Ar purge.

tion/reduction of more IrO₂ particles or the facilitation of surface ceria reduction in the presence of Ir.

The hydrogen consumption for the Ir/Ce sample considerably exceeds the theoretical value required for complete reduction of IrO₂ (52 μmol H₂ g^{−1}). This was found to be 89.7 μmol g^{−1}, a value that clearly implies the contribution from surface CeO₂ reduction (first peak at 216 °C), in line with relevant literature studies [58,59]; partial surface reduction of CeO₂ through H₂ spillover from the Ir metal to the support surface.

3.1.5. CO chemisorption-DRIFTS studies

To reveal the impact of CeO₂-induced modifications on the surface chemistry of Ir/AlCe catalyst, *in situ* DRIFTS-CO chemisorption studies were carried out. Fig. 5 shows DRIFT spectra recorded in the νC–O stretching vibrational mode region for the Ir/Al, Ir/Ce and CeO₂-promoted alumina (Ir/AlCe) catalysts, following CO adsorption (30 min) and Ar purge (5 min) at 30 °C. The Ir/Al and Ir/Ce catalysts present one main infrared absorption band centered at 2060 cm^{−1}, which is assigned to linearly adsorbed CO (L-CO) on Ir⁰ (reduced) sites [53,60–67]. Whereas an infrared band centered at 1860 cm^{−1} was only observed in the case of Ir/Ce catalyst (Fig. 5). The latter IR band is associated with bridged CO species (B-CO) [53,63,67–69]. Taking into account the fact that no oxidized Ir species were identified by CO-DRIFTS, as opposed to the Ir/AlCe catalyst (see below), this could imply that after hydrogen reduction at 300 °C and CO treatment at 30 °C, Ir⁰ (reduced) sites prevail on the catalyst surface of Ir/Al and Ir/Ce solids leading only to the formation of L-CO species (IR band at 2060 cm^{−1}). The latter is in harmony with the CO-DRIFTS results reported by Iojoiu *et al* [62] on Ir/γ-Al₂O₃ after oxidation followed by hydrogen reduction.

CeO₂ modification of γ-Al₂O₃ support (Ir/AlCe catalyst) results in significant alterations in the CO chemisorption behavior of iridium surface. In particular, three infrared bands can be observed, namely: an intense band at 2064 cm^{−1} with a shoulder in the 2000–2010 cm^{−1} range, and a small IR band at 1847 cm^{−1}. The

first band has been already assigned to L-CO species on Ir⁰ (reduced) sites, whereas the shoulder is attributed to *gem*-dicarbonyl adsorbed CO on partially oxidized iridium (Ir^{δ+}(CO)₂, G-CO) on very small particles [63]. It was reported [63] that the main difference between single-crystal studies and supported Ir catalysts is the presence of G-CO either alone or in the presence of L-CO species. The ratio between the intensities of the IR bands of the L-CO and G-CO depends on several parameters such as the metal loading, the nature of the support and the reduction temperature [63]. It is to be mentioned here that G-CO species provides two IR bands, the symmetric (~2070–2080 cm⁻¹) and antisymmetric (~2010 cm⁻¹) dicarbonyl vibrations [67,68]. The IR band centered at 2064 cm⁻¹ is, therefore, the overlap of the ν(L-CO) and ν(G-CO)_s bands. The IR band centred at 1847 cm⁻¹ is assigned to bridged CO species (B-CO) [53,63,66]. The slight shift of this band to lower wavenumbers with respect to that observed in the Ir/Ce solid might be explained as due either to a surface coverage difference, or to an inherent small C–O binding energy difference between the two B-CO species populated on Ir/Ce and Ir/AlCe solids.

It is worth mentioning that after hydrogen reduction treatment carried out prior to CO chemisorption, the ceria-promoted Ir/AlCe catalyst exhibits oxidized Ir species as opposed to the non-promoted Ir/Al and the Ir/Ce catalysts, in which iridium largely exists in metallic state (G-CO species were hardly observed, Fig. 5). These results in conjunction with the TEM/STEM and H₂-TPR analyses imply the formation of oxidized Ir crystallites in the Ir/AlCe catalyst sample, which persist hydrogen reduction at 300 °C. According to the HAADF-STEM results previously presented and discussed, the AlCe support surface promoted the formation of a large number density of very small Ir particles of metallic character, as in the case of bare Al support. However, these very small Ir particles appear to possess Ir^{δ+} sites in the case of Ir/AlCe, very likely at the Ir-CeO₂ support interface, and which persist H₂ reduction. Such sites couldn't be identified by the electron spectroscopy techniques used here. The very small Ir particles appeared in Ir/AlCe are likely strongly bound on the Ce support surface *via* oxygen-bridging (Ce–O–Ir). The latter was previously related to the second H₂-TPR peak (350–500 °C range).

The above mentioned view of Ir^{δ+} sites formation finds strong support in the DRIFTS-CO chemisorption studies (Fig. 5). It is very interesting to note here that the formation of such very small Ir particles in the AlCe support is the result of the co-precipitation synthesis method applied. The existence of some surface interaction between the ceria and alumina particles, which might have created specific sites for Ir deposition in very small particles, cannot be excluded.

Fig. 6 shows DRIFTS-CO spectra recorded at 30, 200 and 400 °C under Ar gas flow during TPD (see Section 2.2) over the Ir/AlCe catalyst. It is clearly indicated that L-CO (2064 cm⁻¹) is less thermally stable than the G-CO (2004 cm⁻¹) and B-CO (1847 cm⁻¹), where the L-CO desorbs completely at T ~400 °C and the latter two species persist even at 400 °C. This result is in agreement with previous reports [63,69], where stable G-CO adsorbed species (~2000 cm⁻¹) were observed at high-T on Ir containing solids. In Fig. 6, the symmetric G-CO band (~2070–2080 cm⁻¹) overlapped with the L-CO at 2064 cm⁻¹ and that of (G-CO)_{as} recorded at 30 °C have shifted to lower wavenumbers at 400 °C (Fig. 6) due to the significant decrease in the surface coverage of G-CO species. Similar DRIFTS-CO TPD spectra were also recorded on the Ir/Al and Ir/Ce solids. It was found that the ratio of L-CO (T)/L-CO (30 °C) was 0.51 and 0.25 at 200 °C for the Ir/Ce and Ir/Al catalyst, respectively, whereas the same ratio was found to be 0.25 and 0.12 at 400 °C. This important result probes for the different adsorption and desorption characteristics of the Ir⁰ sites in the two catalytic surfaces. Due to the overlapping of ν(L-CO) and ν(G-CO)_s in the Ir/AlCe solid, it was difficult to obtain a reli-

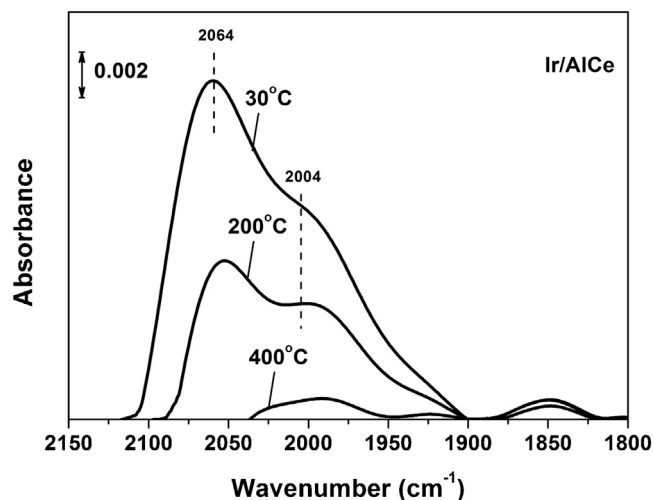


Fig. 6. *In situ* DRIFTS-CO spectra recorded on Ir/AlCe catalyst in Ar gas flow at 30 °C (following 1 vol% CO/He gas treatment at 30 °C) and after TPD at 200 and 400 °C (see Section 2.2).

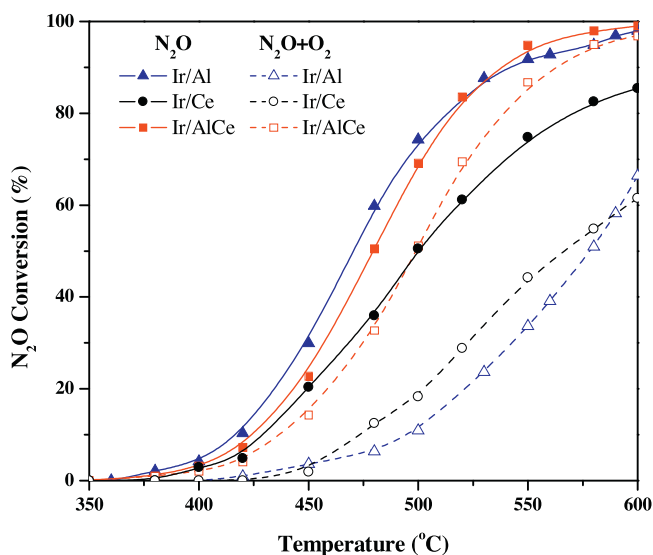


Fig. 7. N₂O conversion vs. T profiles (350–600 °C range) over supported Ir (0.5 wt%) catalysts in the absence and presence of O₂ in the feed stream. Feed gas composition: 1000 ppm N₂O, zero or 2 vol% O₂ in He; GHSV = 40,000 h⁻¹.

able value for the same L-CO (T)/L-CO (30 °C) ratio in this catalytic system.

3.2. deN₂O catalytic activity

Fig. 7 presents the effect of CeO₂ on the deN₂O activity of supported Ir catalysts in terms of N₂O conversion in the 350–600 °C range. The obtained results reveal that in the absence of O₂ in the feed stream (1000 ppm N₂O/He), the incorporation of CeO₂ in the γ-Al₂O₃ support composition does not practically affect the N₂O decomposition activity behavior. Both Ir/Al and Ir/AlCe catalysts demonstrate similar N₂O conversion vs. T profiles, where almost complete N₂O conversion at ca. 600 °C is achieved. An inferior activity was obtained for the Ir/Ce catalyst, where ~85% N₂O conversion was attained at 600 °C. However, under excess O₂ reaction conditions (1000 ppm N₂O/2 vol% O₂/He), a completely different behavior is obtained. The deN₂O activity of both the Ir/Al and Ir/Ce catalysts is largely decreased by the presence of oxygen, as indicated also by the upward shift of the conversion profile (ca. T₅₀

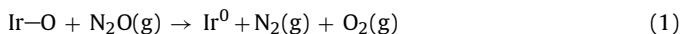
by up to 100 °C). On the contrary, the deN₂O efficiency of CeO₂-promoted Ir/AlCe catalyst is only slightly affected by the presence of oxygen in the feed stream. These results indicate the existence of a synergistic effect between CeO₂ and Al₂O₃ upon Ir (0.5 wt%) addition.

4. Discussion

The deN₂O catalytic activity of the Ir/Al, Ir/Ce and Ir/AlCe solids in the presence and absence of oxygen in the feed stream can be understood to a good extent considering three important factors that influence the integral rate of N₂O decomposition depicted in Fig. 7. The first factor is the *site reactivity* and how this is influenced by the local surface structure of Ir particles/clusters (e.g. kind of crystal face, Ir co-ordination number and electron density). This factor may appear to be different for the three catalytic systems investigated according to the HAADF-STEM studies (Figs. 2 and 3). The second factor is the *concentration of such active sites per gram of catalyst* for the same Ir loading (0.5 wt%) present in each catalytic system. This parameter can only be determined by SSITKA-Mass spectrometry studies [70], subject that was out of the scope of the present work. The third factor is the *effect of gaseous/adsorbed and support oxygen* on main kinetic/mechanistic issues of the N₂O decomposition reaction at hand for each of the supported Ir catalytic surfaces. These important issues are discussed in what follows.

The high catalytic activity for N₂O decomposition on the Rh/CeO₂ compared to Rh/γ-Al₂O₃ was reported some years ago [71], where it was proposed that this is largely due to the formation of electron rich sites at the interface between the dispersed Rh particles (partially oxidized) and the ceria support. Important issues of the N₂O decomposition mechanisms over the same catalytic systems were recently reported [72] based on elegant transient isotopic experiments (use of ¹⁵N₂¹⁸O and ¹⁸O₂) coupled with *in situ* spectroscopic studies (DRIFTS, XPS). The main conclusions reached were that N₂O decomposition is largely catalysed by Rh⁰ (reduced) sites in the case of Rh/γ-Al₂O₃, where in the case of Rh/CeO₂, the support strongly interacts with Rh, and as a result of this very small oxidized Rh particles (Rh³⁺ species) are stabilised during N₂O decomposition. In the case of Rh/CeO₂, the active sites are located on Rh and along the Rh-ceria interface or within a small region around the interface. In a similar manner, it has been clearly shown [19] that Rh^{δ+} species, stabilised *via* metal-support interactions, are more active than metallic Rh (Rh⁰) for N₂O decomposition over Rh supported on La- or Pr-doped CeO₂.

In the case of Ir/γ-Al₂O₃ (Ir/Al) catalyst of the present work, the following basic redox chemical reaction steps are proposed, based on which the X_{N2O} vs. T profiles (Fig. 7) can be explained.



In the absence of convincing evidence that removal of adsorbed oxygen from the oxidized iridium surface should proceed only *via* reaction step (3) (L-H mechanism), then reaction step (1) can also proceed (Eley-Rideal mechanism). In fact, the latter mechanism was proved to be the dominant one on Rh/CeO₂ [72] after providing strong evidence based on isotopic and XPS studies. The rate of N₂O decomposition is, therefore, controlled by the slowest step of this redox mechanism (steps (1)–(2)). Any structure sensitivity of the N₂O decomposition rate on the most stable Ir crystallographic faces should definitely become another important factor to consider for a better understanding

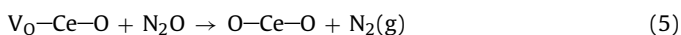
of the Ir particle size effect on the present supported Ir surfaces. According to our knowledge, such information is not yet available.

On the basis of the above discussion and the suggested mechanism of N₂O decomposition on Ir/Al catalyst, the negative effect of the presence of 2 vol% O₂ in the feed of 1000 ppm N₂O/He (Fig. 7) on the integral reaction rate is proposed to be the result of a reduced concentration of Ir⁰ sites under N₂O/O₂/He compared to N₂O/He steady-state reaction conditions, where Ir⁰ sites seem to provide a less energetic pathway for N₂O decomposition compared to reaction step (1). The latter parameter is regulated by the relative rates of reaction steps (1)–(3) and, therefore, by the kinetics governing each of these reaction steps. It is apparent that the backward rate of reaction step (3) becomes important, limiting the availability of Ir⁰ sites. In fact, a large increase in the rate of N₂O decomposition is observed in the 525–600 °C range which is not observed in the case of N₂O/He reaction, result that might be explained to be partly due to the significant increase of the forward rate of reaction step (3) (desorption of O-s on the Ir surface and not decomposition of bulk IrO₂).

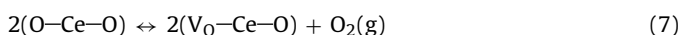
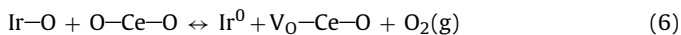
The participation of ceria support in the N₂O decomposition reaction over Rh/CeO₂ was proved to be the result of labile oxygen transfer from ceria to Rh at the metal-support interface, or within a short region around this interface [72]. This mechanistic step is also proposed to occur in the present Ir/CeO₂ catalytic system (Ir/Ce) but also to the Ir/AlCe one, where for the latter a large number of isolated very small particles deposited on CeO₂ primary crystals were identified by HAADF-STEM. This oxygen back-spillover process can be presented by the following chemical step (4):



where V₀ is an oxygen vacant site (enrich with electron density left behind by the removal of oxygen atom). The resulting reduced ceria can then be re-oxidized by N₂O according to the following elementary reaction step (5):



The interaction of N₂O with the V₀-Ce-O site might occur *via* an Eley-Rideal step (N₂O(g) is invoked in step (5)) or a Langmuir-Hinshelwood mechanism, where adsorbed N₂O-s on Ir^{δ+} (or Ir⁰) sites at the iridium-ceria interface must be invoked. The catalytic cycle is completed by the removal of adsorbed oxygen from the Ir surface *via* step (3) or step (6), or even *via* desorption of di-oxygen from the ceria surface (step (7)). The latter step is likely to occur at high temperatures.



The above described mechanistic sequence (steps (4)–(7)) is further supported by the present H₂-TPR results on Ir/Ce (Fig. 4, Table 1), where besides the reduction of IrO₂ particles, an increased concentration of labile oxygen is formed at the metal-support interface. It has been recently revealed by means of XPS and Raman studies that addition of Ir to ceria leads to the formation of surface oxygen vacancies, thus to a reduced ceria, where Ir^{x+}-O²⁻-Ce³⁺ surface entities in the ceria crystallites were suggested [73]. Moreover, it has been demonstrated by means of OSC measurements that oxygen uptake (due to the oxygen vacancies formed) is increased by 2–3 times upon the incorporation of Ir in ceria [74,75].

On the basis of the above described important mechanistic steps for N₂O decomposition on supported Ir⁰/Ir^{δ+} surfaces, the X_{N2O} vs.

T activity profiles of CeO₂-based supported Ir (Fig. 7) can now be understood to a good extent. First of all, it should be noted that the Ir/Ce and Ir/AlCe catalysts contain a wide and different in size distribution of IrO₂ particles, as a consequence of the surface properties of CeO₂ and Al₂O₃-CeO₂ supports prepared by the co-precipitation method, and the impregnation and calcination (600 °C) experimental conditions applied. Furthermore, the Ir/AlCe contains a large number density of very small particles of Ir deposited on the ceria surface (HAADF-STEM studies), the latter being oxidized by the ceria support according to the CO-DRIFTS experimental results (Figs. 5 and 6). It should be re-emphasized at this point that these partially oxidized Ir^{δ+} species resist on their full reduction in hydrogen, result that was observed only in the Ir/AlCe and not in the Ir/Al or Ir/Ce catalysts. The probability that in the case of Ir/CeO₂ catalyst some Ir is in the oxidized state (Ir^{δ+}) under N₂O/O₂ reaction conditions cannot be excluded, in spite of the fact that these sites are reduced in hydrogen at 300 °C, according to the CO-DRIFTS results (Figs. 5 and 6).

The remarkable resistance towards the loss of deN₂O activity in the presence of oxygen observed in the case of Ir/AlCe compared to Ir/Al and Ir/Ce catalytic systems (Fig. 7) must be due to the following reasons according to the mechanistic steps (4)–(7). The rate of N₂O decomposition seems to be largely determined by a significant number of Ir^{δ+} sites formed along the Ir-ceria interface, which provide favourable pathway for N₂ formation (steps (4)–(5)), thus possessing a higher site reactivity. The backward rates of steps (6) and (7) seem to be suppressed, thus the concentration of oxygen vacancies (in the absence or presence of gaseous oxygen) is little affected, the latter being the key intermediate for N₂O decomposition. This mechanistic route is not available in the case of Ir/Al catalyst, the activity of which is largely reduced in the presence of O₂(g) as previously explained. In the case of Ir/Ce catalyst, the lower availability of Ir⁰/Ir^{δ+} redox pairs (revealed by CO-DRIFTS, Fig. 5) seems to be detrimental for the N₂O decomposition activity, on the basis of the redox mechanism proposed. To this end, it has been recently shown [15] that the high deN₂O activity of Cu/CeO₂ samples prepared by co-precipitation could be associated with the increased concentration and reactivity of Ce⁴⁺/Ce³⁺ and Cu²⁺/Cu⁺ redox pair sites.

As suggested by Xue et al. [76], metal cationic centres provide electron density to the antibonding orbital of N₂O, and any electronic promoter on the surface of a deN₂O catalyst would enhance decomposition of N₂O. In the case of Ir/AlCe, the available electron density in the V_O site per Ir atom, at the iridium-ceria interface, is likely to be larger compared to that in Ir/Ce. Hong et al. [64] have reported a very interesting work on the effect of Ir loading on the selective hydrogenation of crotonaldehyde over Ir/SiO₂ catalysts. The authors concluded that the low-loading (1 wt% Ir/SiO₂) catalyst contained predominantly surface Ir^{δ+} species, whereas higher Ir loadings (3–5 wt%) contained a mixture of Ir⁰ and Ir^{δ+} species, the latter being twice as active than those formed in the low-loading catalysts. The authors concluded that a proper Ir^{δ+}/Ir⁰ ratio may be suitable for the chemisorption and activation of the crotonaldehyde molecule. In a similar manner, it was found that the activity of Ir-based catalysts is notably enhanced after high-temperature treatment, which results in the establishment of an optimal Ir^{δ+}/Ir⁰ ratio [19].

In order to fully understand the deN₂O performance of the three catalytic systems (Fig. 7), it is imperative to know the concentration of active sites and the site reactivity of each catalytic surface, as noted in a previous paragraph, subject that has been recently elucidated in some detail for the case of WGS reaction on ceria-supported Pt catalysts [77–80]. In the light of the discussion offered above, it could be stated that the design of an efficient supported Ir catalyst may require the formation of very small Ir particles with an opti-

mum Ir^{δ+}/Ir⁰ atom ratio in order to achieve a high and stable deN₂O performance under oxidizing conditions.

5. Conclusions

The effects of CeO₂ in the Al₂O₃-20 wt% CeO₂ support prepared by the co-precipitation method on the Ir particle size, morphology and oxidation state, and in turn on the deN₂O catalytic activity of supported Ir were investigated. The obtained results revealed that in the absence of O₂ (1000 ppm N₂O/He) both the non-promoted and CeO₂-promoted Ir supported catalysts demonstrate similar deN₂O activity behavior. However, in the presence of excess O₂ (1000 ppm N₂O/2 vol% O₂/He), the activity behavior of Ir/Al and Ir/Ce catalysts was drastically hindered as opposed to the stable performance of CeO₂-promoted Ir/Al catalyst (Ir/AlCe). The superiority of the latter catalytic composition was interpreted on the basis of HAADF-STEM, H₂-TPR and CO-DRIFTS experiments. The establishment of a certain Ir^{δ+}/Ir⁰ ratio and oxygen vacant sites (V_O) concentration in ceria around very small supported Ir particles under oxidative reaction conditions seem to largely promote a sustainable N₂O adsorption and decomposition into N₂ and O₂ over the CeO₂-promoted Ir/Al catalyst. In the case of Ir/Al, a different deN₂O decomposition mechanism occurs, where the site reactivity of Ir^{δ+}/Ir⁰ established under oxidizing conditions is reduced significantly.

Acknowledgements

This research has been co-financed by the European Union (European Social Fund) and Greek national funds through the Operational Program “Education and Lifelong Learning” of the National Strategic Reference Framework (NSRF)-Research Funding Program: THALES-Investing in knowledge society through the European Social Fund (MIS 375643). This work has also received funding from the European Union, 7th Framework Programme (Grant Agreement 312483—ESTEEM2 (Integrated Infrastructure Initiative-I3)). A.D. greatly acknowledges F. Schmidt, W. Grogger and F. Hofer from the TU of Graz for the acquisition of EELS spectra and fruitful discussions.

References

- [1] L. Li, J. Xu, J. Hu, J. Han, *Environ. Sci. Technol.* 48 (2014) 5290–5297.
- [2] M. Konsolakis, *ACS Catal.* 5 (2015) 6397–6421.
- [3] A.R. Ravishankara, M.A., Sutton, E.A., Davidson, D., Kanter, J.S. Daniel, Chapter 1, A UNEP Synthesis Report (2013).
- [4] A.R. Ravishankara, J.S. Daniel, R.W. Portmann, *Science* 326 (2009) 123.
- [5] S. Parres-Escápez, M.J. Illán-Gómez, C. Salinas-Martínez de Lecea, A. Bueno-López, *Appl. Catal. B: Environ.* 96 (2010) 370–378.
- [6] N.W. Cant, D.E. Angove, D.C. Chambers, *Appl. Catal. B: Environ.* 17 (1998) 63–73.
- [7] F. Kapteijn, J. Rodriguez-Mirasol, J.A. Moulijn, *Appl. Catal. B: Environ.* 9 (1996) 25–64.
- [8] A. Shimizu, K. Tanaka, M. Fujimori, *Chemosphere-Global Change Sci.* 2 (2000) 425–434.
- [9] G. Centi, P. Generali, L. dall’Olio, S. Perathoner, Z. Rak, *Ind. Eng. Chem. Res.* 39 (2000) 131–137.
- [10] M.A. Wojtowicz, F.P. Miknis, R.W. Grimes, W.W. Smith, M.A. Serio, J. Hazard. Mater. 74 (2000) 81–89.
- [11] J. Perez-Ramirez, F. Kapteijn, K. Schoffele, J.A. Moolijn, *Appl. Catal. B* 44 (2003) 117–151.
- [12] G. Centi, S. Perathoner, F. Vazzana, M. Marella, M. Tomaselli, M. Mantegazza, *Adv. Environ. Res.* 4 (2000) 325–338.
- [13] M. Konsolakis, F. Aligizou, G. Goula, I.V. Yentekakis, *Chem. Eng. J.* 230 (2013) 286–295.
- [14] P. Granger, P. Malfroy, G. Leclercq, *J. Catal.* 223 (2004) 142–151.
- [15] M. Konsolakis, S.A.C. Carabineiro, E. Papista, G.E. Marnellos, P.B. Tavares, J. Agostinho Moreira, Y. Romaguera-Barcelay, J.L. Figueiredo, *Catal. Sci. Technol.* 5 (2015) 3714–3727.
- [16] J.N. Armor, T.A. Braymer, T.S. Farris, Y. Li, F.P. Petrocchi, E.L. Weist, S. Kannan, C.S. Swamy, *Appl. Catal. B: Environ.* 7 (1996) 397–406.
- [17] G. Delahay, M. Mauvezin, A. Guzman-Vargas, B. Coq, *Catal. Commun.* 3 (2002) 385–389.

- [18] G. Centi, A. Galli, B. Montanari, S. Perathoner, A. Vaccari, *Catal. Today* 35 (1997) 113–120.
- [19] A. Bueno-Lopez, I. Such-Basanez, C. Salinas-Martinez de Lecea, J. Catal. 244 (2006) 102–112.
- [20] Y.D. Scherson, S.J. Aboud, J. Wilcox, B.J. Cantwell, *J. Phys. Chem. C* 115 (2011) 11036–11044.
- [21] R. Burch, S.T. Daniells, J.P. Breen, P. Hu, *J. Catal.* 224 (2004) 252–260.
- [22] R. Burch, S.T. Daniells, J.P. Breen, P. Hu, *Catal. Lett.* 94 (2004) 103–108.
- [23] M. Ogura, A. Kawamura, M. Matsukata, E. Kikuchi, *Chem. Lett.* 29 (2000) 146–147.
- [24] T. Nakatsuji, *Appl. Catal. B: Environ.* 25 (2000) 163–179.
- [25] M. Nawdali, H. Praliaud, M. Primet, *Top. Catal.* 16 (2001) 199–204.
- [26] C. Wogerbauer, M. Maciejewski, A. Baiker, *Appl. Catal. B: Environ.* 34 (2001) 11–27.
- [27] A.Q. Wang, D.B. Liang, C.H. Xu, X.Y. Sun, T. Zhang, *Appl. Catal. B: Environ.* 32 (2001) 205–212.
- [28] C. Wogerbauer, M. Maciejewski, A. Baiker, *J. Catal.* 205 (2002) 157–167.
- [29] A.Q. Wang, L. Ma, Y. Cong, T. Zhang, D.B. Liang, *Appl. Catal. B: Environ.* 40 (2003) 319–329.
- [30] M. Haneda, T. Yoshinari, K. Sato, Y. Kintaichia, H. Hamada, *Chem. Commun.* (2003) 2814–2815.
- [31] M.D. Amiridis, C. Mihut, M. Maciejewski, A. Baiker, *Top. Catal.* 28 (2004) 141–149.
- [32] M. Haneda, Pusparatu, Y. Kintaichi, I. Nakamura, M. Sasaki, T. Fujitani, H. Hamada, *J. Catal.* 229 (2005) 197–205.
- [33] T. Nanba, S. Shinohara, S. Masukawa, J. Uchisawa, A. Ohi, A. Obuchi, *Appl. Catal. B: Environ.* 84 (2008) 420–425.
- [34] T. Fujitani, I. Nakamura, A. Takahashi, M. Haneda, H. Hamada, *J. Catal.* 253 (2008) 139–147.
- [35] H. Inomata, M. Shimokawabe, A. Kuwana, M. Arai, *Appl. Catal. B: Environ.* 84 (2008) 783–789.
- [36] M. Haneda, H. Hamada, *J. Catal.* 273 (2010) 39–49.
- [37] M. Haneda, N. Aoki, M. Sasaki, H. Hamada, M. Ozawa, *Appl. Catal. A: Gen.* 394 (2011) 239–244.
- [38] T. Fujitani, I. Nakamura, Y. Kobayashi, A. Takahashi, M. Haneda, H. Hamada, *J. Phys. Chem. B* 109 (2005) 17603–17607.
- [39] W.H. Chen, T.E. Madey, A.L. Stottlemeyer, J.G. Chen, P. Kaghazchi, T. Jacob, *J. Phys. Chem. C* 112 (2008) 19113–19120.
- [40] W.H. Chen, A.L. Stottlemeyer, J.G. Chen, P. Kaghazchi, T. Jacob, T.E. Madey, R.A. Bartynski, *Surf. Sci.* 603 (2009) 3136–3144.
- [41] J. Haber, M. Nattich, T. Machej, *Appl. Catal. B: Environ.* 77 (2008) 278–283.
- [42] M. Konsolakis, C. Drosou, I.V. Yentekakis, *Appl. Catal. B: Environ.* 123–124 (2012) 405–413.
- [43] N. Pasha, N. Lingaiah, P.S.S. Reddy, P.S.S. Prasad, *Catal. Lett.* 118 (2007) 64–68.
- [44] S. Parres-Esclapez, F.E. López-Suárez, A. Bueno-López, M.J. Illán-Gómez, B. Ura, J. Trawczynski, *Top. Catal.* 52 (2009) 1832–1836.
- [45] G. Pekridis, N. Kaklidis, M. Konsolakis, E.F. Iliopoulou, I.V. Yentekakis, G.E. Marnellos, *Top. Catal.* 54 (2011) 1135–1142.
- [46] A. Papavasiliou, A. Tsetsekou, V. Matsouka, M. Konsolakis, I.V. Yentekakis, N. Boukos, *Appl. Catal. B* 106 (2011) 228–241.
- [47] E.F. Iliopoulou, E.A. Efthimiadis, L. Nalbandian, I.A. Vasalos, J.O. Barth, J.A. Lercher, *Appl. Catal. B: Environ.* 60 (2005) 277–288.
- [48] E. Pachatouridou, E. Papista, E.F. Iliopoulou, A. Delimitis, G. Goula, I.V. Yentekakis, G.E. Marnellos, M. Konsolakis, *J. Environ. Chem. Eng.* 3 (2015) 815–821.
- [49] C. Jehn, R. Völker, M.I. Ismail, *Platinum Met. Rev.* 22 (1978) 92–97.
- [50] T. Hou, Y. Lei, S. Zhang, J. Zhang, W. Cai, *J. Rare Earths* 33 (2015) 42.
- [51] W.K. Jóźwiak, T.P. Maniecki, *Thermochim. Acta* 435 (2005) 151–161.
- [52] F. Wang, W. Cai, Tana, H. Provendier, Y. Schuurman, C. Descorme, C. Mirodatos, W. Shen, *Appl. Catal. B: Environ.* 125 (2012) 546–555.
- [53] P. Chen, J. Lu, G. Xie, L. Zhu, M. Luo, *React. Kinet. Mech. Catal.* 106 (2012) 419–434.
- [54] M.A. Vicerich, V.M. Benitez, C. Especel, F. Epron, C.L. Pieck, *Appl. Catal. A: Gen.* 453 (2013) 167–174.
- [55] C. Carnevillier, F. Epron, P. Marecot, *Appl. Catal. A: Gen.* 275 (2004) 25–33.
- [56] H. Tian, Y. Zhang, X. Sun, D. Liang, L. Lin, *Appl. Catal. A: Gen.* 210 (2001) 55–62.
- [57] X. Hong, B. Li, Y. Wang, J. Lu, G. Hu, M. Luo, *Appl. Surf. Sci.* 270 (2013) 388–394.
- [58] C. de Leitenburg, A. Trovarelli, J. Kaspert, *J. Catal.* 166 (1997) 98–107.
- [59] W. Cai, F. Wang, C. Daniel, A.C. van Veen, Y. Schuurman, C. Descorme, H. Provendier, W. Shen, C. Mirodatos, *J. Catal.* 286 (2012) 137–152.
- [60] A. Erdohelyi, K. Fodor, G. Suru, *Appl. Catal. A: Gen.* 139 (1996) 131–147.
- [61] H. Rojas, G. Diaz, J.J. Martinez, C. Castaneda, A. Gomez-Cortes, J. Arenas-Alatorre, *J. Mol. Catal. A: Chem.* 363 (2012) 122–128.
- [62] E. Jojoiu, P. Gelin, H. Praliaud, M. Primet, *Appl. Catal. A: Gen.* 263 (2004) 39–48.
- [63] A. Bourane, M. Nawdali, D. Bianchi, *J. Phys. Chem. B* 106 (2002) 2665–2671.
- [64] X. Hong, B. Li, Y. Wang, J. Lu, G. Hu, M. Luo, *Appl. Surf. Sci.* 270 (2013) 388–394.
- [65] P. Chen, J.-Q. Lu, G.-Q. Xie, G.-S. Hu, L. Zhu, L.-F. Luo, W.-X. Huang, M.-F. Luo, *Appl. Catal. A: Gen.* 433–434 (2012) 236–242.
- [66] T.-S. Nguyen, F. Morfin, M. Aouine, F. Bosselet, J.-L. Rousset, L. Piccolo, *Catal. Today* 253 (2015) 106–114.
- [67] Y.M. López-De Jesús, A. Vicente, G. Lafaye, P. Marécot, C.T. Williams, *J. Phys. Chem. C* 112 (2008) 13837–13845.
- [68] F. Solymosi, É. Novák, A. Molnár, *J. Phys. Chem.* 94 (1990) 7250–7255.
- [69] O. Alexeev, B.C. Gates, *J. Catal.* 176 (1998) 310.
- [70] A.M. Efstathiou, J.T. Gleaves, G.S. Yablonsky, in: M. Che, J.C. Vedrine (Eds.), *Characterization of Solid Materials: From Structure to Surface Reactivity*, vol. 2, Wiley-VCH Weinheim, Germany, 2012, pp. 1013–1073 (Chapter 22).
- [71] J. Cunningham, J.N. Hickey, R. Cataluna, J.C. Conesa, J. Soria, A. Martinez-Arias, *Stud. Surf. Sci. Catal.* 101 (1996) 681.
- [72] S. Parres-Esclapez, Ph.D. thesis, Universida de Alicante, 2011.
- [73] T.-S. Nguyen, G. Postole, S. Lorient, F. Bosselet, L. Burel, M. Aouine, L. Massin, P. Gelin, F. Morfin, L. Piccolo, *J. Mater. Chem. A* 2 (2014) 19822–19832.
- [74] J. Mikulová, J. Barbier Jr., S. Rossignol, D. Mesnard, D. Duprez, C. Kappenstein, *J. Catal.* 251 (2007) 172–181.
- [75] E.M. Sadovskaya, Y.A. Ivanova, L.G. Pinaeva, G. Grasso, T.G. Kuznetsova, A. van Veen, C. Mirodatos, *J. Phys. Chem. A* 111 (2007) 4498.
- [76] L. Xue, H. He, C. Lin, C. Zhang, B. Zhang, *Environ. Sci. Technol.* 43 (2009) 890–895.
- [77] C.M. Kalamaras, D. Dionysiou, A.M. Efstathiou, *ACS Catal.* 2 (2012) 2729–2742.
- [78] C.M. Kalamaras, K.C. Petalidou, A.M. Efstathiou, *Appl. Catal. B: Environ.* 136–137 (2013) 225–238.
- [79] A.M. Efstathiou, K.C. Petalidou, *Appl. Catal. B: Environ.* 152–153 (2014) 183–193.
- [80] K.C. Petalidou, C.M. Kalamaras, A.M. Efstathiou, *Catal. Today* 228 (2014) 183–193.